




## Magnetic MOF-808 as a novel adsorbent for toxic metal removal from aqueous solutions†

Cite this: *Environ. Sci.: Adv.*, 2022, 1, 182

Roxana Paz,<sup>a</sup> Herly Viltres,<sup>\*b</sup> Nishesh Kumar Gupta,<sup>cd</sup> Adolfo Romero-Galarza<sup>e</sup> and Carolina Leyva <sup>\*a</sup>

Received 18th January 2022  
Accepted 29th March 2022

DOI: 10.1039/d2va00010e

rsc.li/esadvances

Mercury (Hg) in water is a global concern due to its high toxicity and bioaccumulation in the food chain, which severely affects the environment and human health. In this work, a magnetic zirconium metal–organic framework (Zr-MOF@Fe<sub>3</sub>O<sub>4</sub>) has been synthesized for Hg(II) removal. The Zr-MOF@Fe<sub>3</sub>O<sub>4</sub> demonstrated the maximum adsorption capacity of 303 mg g<sup>-1</sup> at pH 6. The possible mechanism was confirmed by spectroscopic analysis, which indicated that free –COOH groups and Zr–OH were responsible for adsorption. The adsorbent showed high uptake capacity for Hg(II), Pb(II), and Cd(II) ions in a multi-element solution. The regeneration of the material was successfully carried out with NaOH solution for five cycles. Thus, the study has reported a highly efficient adsorbent for the removal of toxic heavy metals from aqueous solutions.

### Environmental significance

Researchers are concerned about water contamination with toxic heavy metals, especially, by lead, mercury, and cadmium poisoning, which is risking millions of lives in rural and semi-urbanized regions of the world. Thus, the decontamination of water for its safe use in drinking and domestic applications needs to be prioritized. Here, we have successfully developed a facile magnetic zirconium-based metal–organic framework composite for simultaneous removal of divalent lead, mercury, and cadmium ions at a near-neutral pH for its application in the treatment of industrial wastewater and groundwater. Imparting magnetism into the metal–organic framework made the phase separation process easy and efficient. The entire water decontamination process was found to be energy-efficient and reversible with the use of affordable NaOH solution as a stripping agent.

## Introduction

Heavy metals are considered one of the most hazardous pollutants in water due to their high toxicity to humans and low biodegradability.<sup>1</sup> One of these metals is mercury, which is a widespread global concern. This pollutant causes serious environmental problems and dangers to human health due to its high toxicity, bio-accumulation, and ability to cause memory loss, Alzheimer's, nephrotic syndrome with high levels of protein in the urine, paralysis coma, and congenital deformities affecting fetuses.<sup>2</sup> The main chemical species of mercury in the environment are the elemental Hg (Hg<sup>0</sup>), inorganic Hg (Hg(II)), and organic forms, primarily methyl-Hg (MeHg). The inorganic

Hg has poor degradability in natural water (or wastewater) and long-range transport in the atmosphere. Also, the Hg(II) species have become the main factor in giving rise to mercury pollution worldwide. For that reason, the World Health Organization (WHO) has set the maximum level of mercury contamination in drinking water at 1 ppb.<sup>3</sup> Therefore, it is a significant challenge for water safety to explore more efficient materials to remove the ultra-low concentration of Hg(II) from contaminated water. The traditional treatment technologies for the removal of mercury include ion exchange,<sup>4</sup> amalgamation,<sup>5</sup> membrane separation,<sup>6</sup> and chemical precipitation.<sup>7</sup> Among these, the most studied technique is adsorption due to its simplicity, high removal efficiency, and affordability.<sup>8–10</sup>

Metal–organic frameworks (MOFs) are materials formed by the coordination of metal ions or metal clusters with organic ligands. MOFs are good candidates for wastewater adsorption treatments, increasing their use in the past decades. Besides, MOFs have important characteristics, such as large specific surface area, designable frame structure, controllable pore size, metal unsaturation sites, and ease of modification.<sup>11,12</sup>

These properties make these materials excellent candidates for metal removal from contaminated water. Modified Zr-MOFs have been showing promising results in the adsorption of highly toxic chemical species such as heavy metal ions like

<sup>a</sup>Instituto Politécnico Nacional, Centro de Investigación en Ciencia Aplicada y Tecnología Avanzada, CDMX, México. E-mail: carolina.leyva.inz@gmail.com

<sup>b</sup>School of Engineering Practice and Technology, McMaster University, Ontario, Canada. E-mail: viltresh@mcmaster.ca

<sup>c</sup>University of Science and Technology (UST), Daejeon, Republic of Korea

<sup>d</sup>Department of Land, Water, and Environment Research, Korea Institute of Civil Engineering and Building Technology (KICT), Goyang, Republic of Korea

<sup>e</sup>Department of Chemical Engineering, School of Chemistry, Universidad Autónoma de Coahuila, México

† Electronic supplementary information (ESI) available. See <https://doi.org/10.1039/d2va00010e>





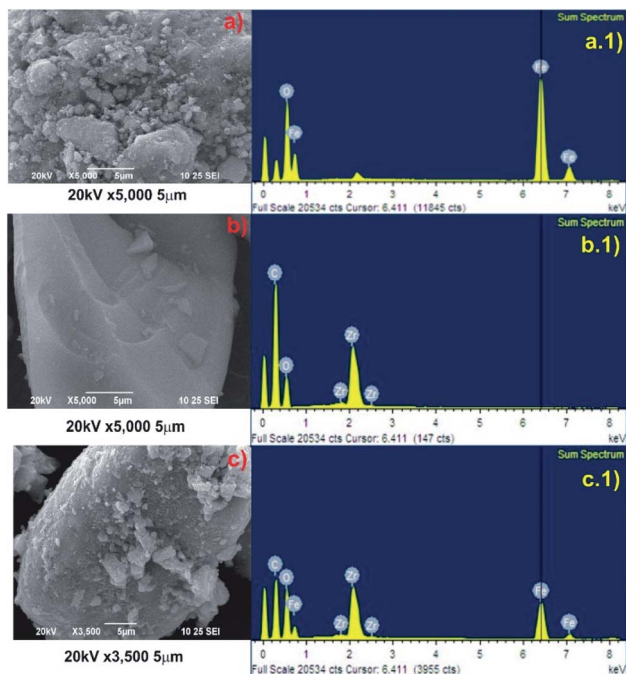


Fig. 1 SEM micrographs and EDAX analysis of (a)  $\text{Fe}_3\text{O}_4$ ; (b) Zr-MOF; (c) Zr-MOF@ $\text{Fe}_3\text{O}_4$ .

peaks of C, O, Fe, and Zr in the spectrum (Fig. 1c.1). The 2D elemental map of Zr-MOF and Zr-MOF@ $\text{Fe}_3\text{O}_4$  is available in Fig. S1.† A uniform distribution of O, C, and Zr was confirmed in the Zr-MOF. In Zr-MOF@ $\text{Fe}_3\text{O}_4$ , a large fraction of the 'Fe' density could be observed over the 'Zr' density in the MOF, which further confirmed the formation of the composite of magnetite and the Zr-MOF.

The PXRD technique provides us with information about the crystallinity and phase purity of the materials (Fig. 2a). The PXRD pattern of the Zr-MOF has a high-intensity peak in the  $5\text{--}15^\circ$  range centred at  $2\theta = 8.2^\circ$  (311 reflection) as opposed to two peaks observed at  $2\theta = 8.3^\circ$  and  $8.7^\circ$  in the reported Zr-trimesate MOF (MOF-808).<sup>17</sup> The broadening of the diffraction peaks was due to the low crystallinity or amorphous nature of the synthesized MOF. In the present study, the use of  $\text{ZrOCl}_2 \cdot 8\text{H}_2\text{O}$  as the Zr precursor was responsible for the low crystallinity of the MOF, which matched with the previously reported work of Ardila-Suárez and co-workers.<sup>18</sup> In the PXRD pattern of  $\text{Fe}_3\text{O}_4$ , the peaks observed at  $2\theta = 30.2^\circ$ ,  $35.5^\circ$ ,  $43.2^\circ$ ,  $53.3^\circ$ , and  $57.1^\circ$  were assigned to the 220, 311, 400, 422, and 511 reflections, respectively, of the cubic inverse spinel structure of the  $\text{Fe}_3\text{O}_4$  phase (JCPDS card#19-0629).<sup>19</sup> The peak for Zr-MOF ( $2\theta = 7.9^\circ$ ), the amorphous feature, and crystalline Bragg reflections of  $\text{Fe}_3\text{O}_4$  is distinctly visible in the diffraction pattern of Zr-MOF@ $\text{Fe}_3\text{O}_4$ , which further confirmed the formation of the magnetic Zr-MOF composite.

The FTIR spectra of Zr-MOF,  $\text{Fe}_3\text{O}_4$ , and Zr-MOF@ $\text{Fe}_3\text{O}_4$  are shown in Fig. 2b. The spectrum of the Zr-MOF shows a broad band at  $3397\text{ cm}^{-1}$  for OH stretching vibrations of Zr-OH and adsorbed water molecules. The band at  $1707\text{ cm}^{-1}$  was due to the unreacted  $-\text{COOH}$  groups in the MOF. The bands at  $1619$

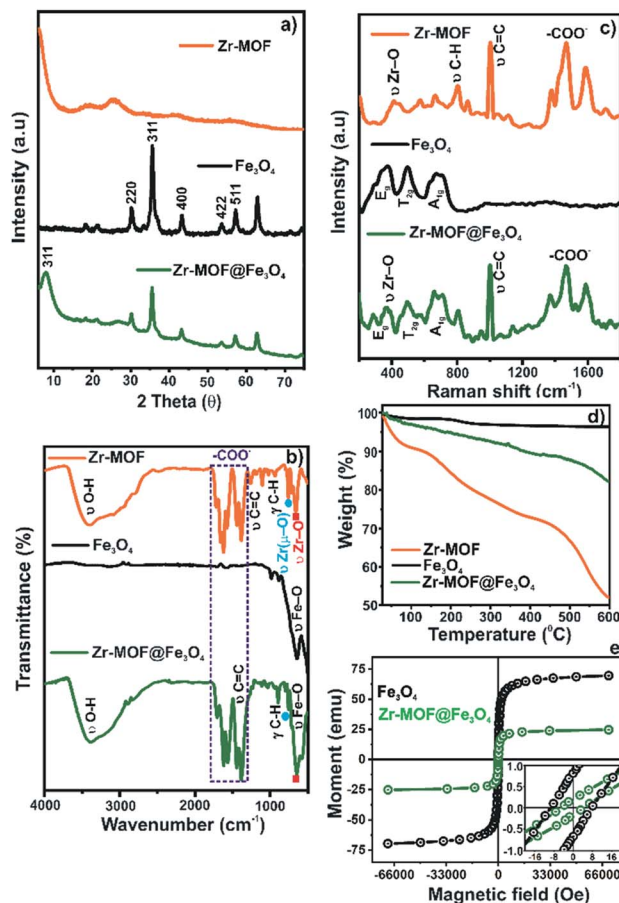


Fig. 2 (a) PXRD patterns; (b) Raman spectra; (c) FTIR spectra; (d) TGA profiles; (e) VSM curves of Zr-MOF,  $\text{Fe}_3\text{O}_4$ , and Zr-MOF@ $\text{Fe}_3\text{O}_4$ .

and  $1387\text{ cm}^{-1}$  were assigned to the asymmetric and symmetric stretching vibrations of Zr-bound carboxylate groups after the coordination process. The band at  $1658\text{ cm}^{-1}$  was attributed to the O-H bending mode of adsorbed water molecules and carbonyl stretching vibrations of guest DMF molecules. The band at  $1446\text{ cm}^{-1}$  was the characteristic band for  $\text{C}=\text{C}$  stretching in the aromatic rings of the ligand.<sup>20,21</sup> Bands observed in the  $1200\text{--}1000$  and  $1000\text{--}700\text{ cm}^{-1}$  range were assigned to the in-plane and out-of-plane C-H bending modes, respectively.<sup>22</sup> The bands at  $647$  and  $460\text{ cm}^{-1}$  were attributed to the stretching modes of the Zr-( $\mu_3\text{-O}$ ) bridges and Zr-O (carboxylate) bonds in the MOF structural framework, respectively.<sup>23</sup> The intense band at  $582\text{ cm}^{-1}$  in the FTIR spectrum of  $\text{Fe}_3\text{O}_4$  was assigned to the O-Fe stretching vibrations.<sup>24</sup> These characteristic bands of Zr-MOF and  $\text{Fe}_3\text{O}_4$  were distinctly visible in the composite, with a slight shift in the energy for carboxylate bands probably due to the weak interaction between the constituents, which confirmed the formation of the magnetic composite.

The Raman spectra of the Zr-MOF,  $\text{Fe}_3\text{O}_4$ , and Zr-MOF@ $\text{Fe}_3\text{O}_4$  are shown in Fig. 2c. In the spectrum of the Zr-MOF, the peak at  $413\text{ cm}^{-1}$  was related to the Zr-O (carboxylate) stretching modes. The peaks at  $803$  and  $868\text{ cm}^{-1}$  were assigned to the C-H bending modes, and the intense  $1005\text{ cm}^{-1}$





peak was associated with the C=C stretching vibrations in the aromatic rings. The peaks at 1589 and 1469  $\text{cm}^{-1}$  were characteristic of asymmetric and symmetric stretching modes of carboxylate bridges, respectively.<sup>25,26</sup> In  $\text{Fe}_3\text{O}_4$ , three bands were observed, where the bands at 374 and 498  $\text{cm}^{-1}$  were assigned to the  $E_g$  and  $T_{2g}(2)$  modes for the symmetric and asymmetric bending of oxygen (concerning Fe) in the tetrahedral void, respectively. The band at 675  $\text{cm}^{-1}$  was due to the  $A_{1g}$  mode for the symmetric stretching of the oxygen atoms in the tetrahedral  $\text{FeO}_4$  groups.<sup>16</sup> The spectral features of  $\text{Fe}_3\text{O}_4$  and Zr-MOF were observed in the Raman spectrum of the Zr-MOF@ $\text{Fe}_3\text{O}_4$  composite.

The TGA profile of materials was recorded in the range of 30–600 °C (Fig. 2d). In the TGA profile of Zr-MOF, three stages of mass loss were noticed in the studied temperature range. The first mass loss, recorded between 30 and 110 °C, was due to the evaporation of physically adsorbed water molecules (9.4% of mass loss). The second mass loss range (110–400 °C, 17.8% of mass loss) was described as the loss of chemisorbed water and physisorbed solvent (DMF/methanol) molecules. The third stage of mass loss (>400 °C) was associated with the thermal degradation of the MOF due to the breakdown of metal-carboxylate coordination bonds.<sup>27,28</sup> Thus, the Zr-MOF was thermally stable up to 400 °C. In the TGA profile of  $\text{Fe}_3\text{O}_4$ , an ~1.5% mass loss below 100 °C was associated with the evaporation of water molecules. In the entire temperature range, an insignificant change in the mass loss confirmed the high thermal stability of the magnetite.<sup>29</sup> The TGA profile of Zr-MOF@ $\text{Fe}_3\text{O}_4$  showed a significantly low mass loss in the entire temperature range compared to the pristine Zr-MOF, which confirmed that the composite was more stable than the Zr-MOF.<sup>16</sup>

The VSM curves of  $\text{Fe}_3\text{O}_4$  and Zr-MOF@ $\text{Fe}_3\text{O}_4$  at 300 K are shown in Fig. 2e. Both materials showed superparamagnetic behaviour with a sigmoidal form, where the remanence was close to zero. The magnetization saturation ( $\mu_s$ ) value of 69.29  $\text{emu g}^{-1}$  for  $\text{Fe}_3\text{O}_4$  decreased to 25.02  $\text{emu g}^{-1}$  for Zr-MOF@ $\text{Fe}_3\text{O}_4$  (Table S2†). The decrease in the  $\mu_s$  value of  $\text{Fe}_3\text{O}_4$  after Zr-MOF addition was due to the increased thickness of the non-magnetic component.<sup>16</sup> Though the  $\mu_s$  value of Zr-MOF@ $\text{Fe}_3\text{O}_4$  was 25.02  $\text{emu g}^{-1}$ , it was sufficient for rapid phase separation from large volumes of water by a strong permanent magnet.

The surface elemental composition and the oxidation states of constituent elements in the materials were confirmed by XPS analysis. The XPS surveys confirmed Zr, C, O, and Fe in the synthesized samples (Fig. 3a and Table S3†). The HRXPS C 1s spectrum of Zr-MOF@ $\text{Fe}_3\text{O}_4$  has four peaks at 284.7, 285.9, 288.6, and 290.7 eV, which were assigned to the  $\text{sp}^2$  C=C (55.8%), C–O (23.4%), O=C=O (16.4%), and  $\pi$ - $\pi^*$  bonding moieties (4.4%) (Fig. 3b and Table S4†).<sup>30</sup> The HRXPS O 1s spectrum has three contributions at 530.2, 531.7, and 533.1 eV, which were due to O–Zr/O–Fe (50.4%), O–C (37.7%), and Zr–OH (11.9%), respectively (Fig. 3c and Table S5†).<sup>31,32</sup> The HRXPS Zr 3d spectrum has two peaks at 182.9 and 185.6 eV for  $3d_{5/2}$  and  $3d_{3/2}$ , respectively, which were assigned to the  $\text{Zr}^{4+}$  oxidation state in the Zr-MOF structure (Fig. 3d).<sup>33</sup> The Zr  $3d_{5/2}$  peak in Zr

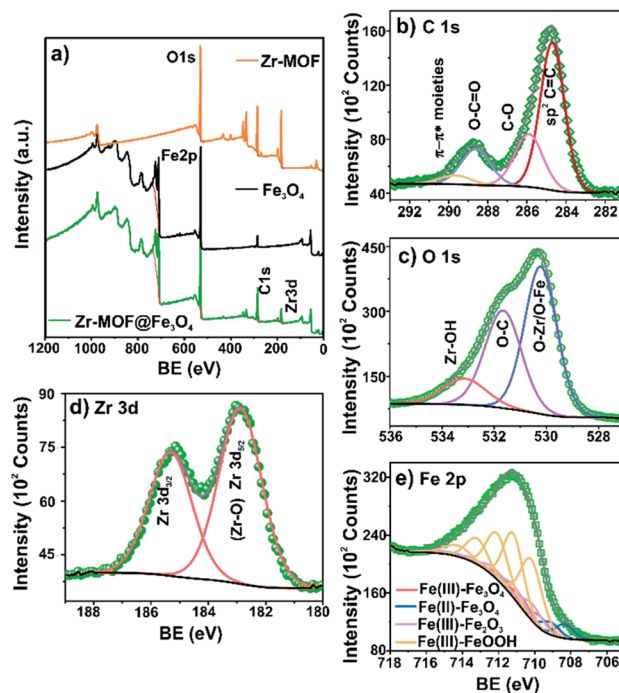


Fig. 3 (a) Survey spectra of Zr-MOF,  $\text{Fe}_3\text{O}_4$ , and Zr-MOF@ $\text{Fe}_3\text{O}_4$ ; high-resolution spectra of (b) C 1s; (c) O 1s; (d) Zr 3d; (e) Fe 2p for Zr-MOF@ $\text{Fe}_3\text{O}_4$ .

salt observed at 183.2 eV shifted to 182.6 eV in the Zr-MOF due to an increase in the electron density around the Zr ions after coordination with the carboxylate groups. This peak in the Zr-MOF shifted to a higher value by 0.3 eV after composite formation, suggesting the possible interaction of Zr-sites with the magnetite surface (Fig. S2 and Table S6†). The high-resolution Fe  $2p_{2/3}$  spectrum of the composite was fitted using the Gupta and Sen multiplets. The resulting fit for Fe  $2p_{3/2}$  confirmed the presence of  $\text{Fe}_3\text{O}_4$  and  $\text{FeOOH}$  components. The  $\text{Fe}^{3+}/\text{Fe}^{2+}$  ratio of 2.2 : 1 in the Zr-MOF@ $\text{Fe}_3\text{O}_4$  was close to the expected ratio of 2.1 : 1 observed for the  $\text{Fe}_3\text{O}_4$  phase (Fig. 3e and Table S7†).<sup>33</sup>

### Parameter optimization

The Hg(II) species adsorption was studied with each component of the final material to find if the magnetic MOF has better performance than each of its components. As observed in Fig. S3,† Zr-MOF@ $\text{Fe}_3\text{O}_4$  showed the best removal efficiency for Hg(II), 97.01%, while  $\text{Fe}_3\text{O}_4$  and Zr-MOF showed 39.35% and 69.71% removal efficiency, respectively. The effect of pH on the Hg(II) adsorption capacity of the composite was studied in the pH 2–6 range (Fig. 4a). The adsorption capacity of 42.1  $\text{mg g}^{-1}$  at pH 2 increased to 48.9  $\text{mg g}^{-1}$  at pH 6. The zeta potential measurements conducted in the pH 2–6 range showed that the surface of the composite was negatively charged. The composite surface becomes more negative with the increasing pH, favouring the adsorption of positively charged Hg(II) ions,<sup>34</sup> with the involvement of physical forces. The adsorption capacity was significantly high in the entire pH range, which suggested its





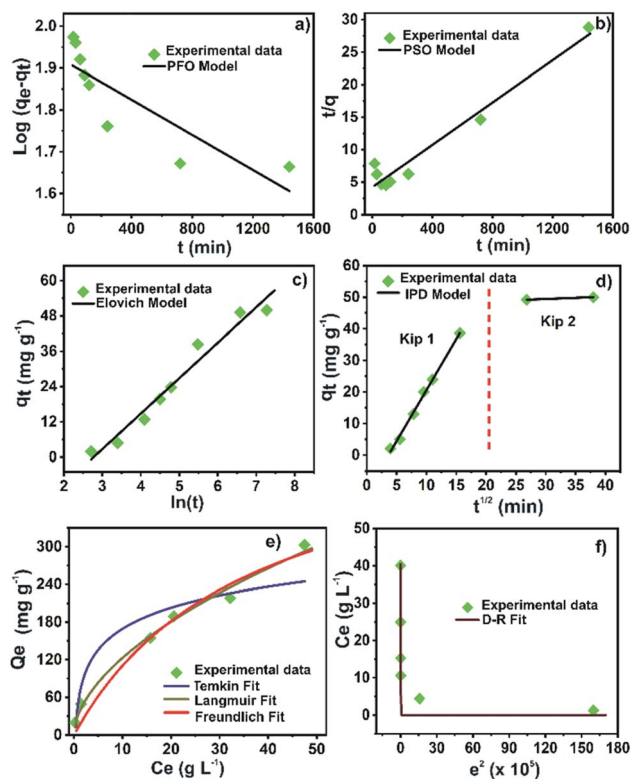


Fig. 6 (a) PFO; (b) PSO; (c) Elovich; (d) IPD kinetic model, (e) Langmuir, Freundlich, and Temkin isotherm fits; (f) Dubinin–Radushkevich isotherm for Hg(II) adsorption onto Zr-MOF@Fe<sub>3</sub>O<sub>4</sub>.

the PSO model. Thus, the adsorption kinetics could be explained by both the Elovich and the PSO kinetic models. Furthermore, the correlation with the PSO model indicated that the adsorption process was mainly controlled by chemisorption, involving valency forces through sharing or exchange of electrons between the metal ions and the adsorbent sites.<sup>40,47</sup> Besides, the Elovich model gave a good correlation for the adsorption on highly heterogeneous surfaces. Moreover, this model showed that chemisorption was a dominant phenomenon along with surface adsorption. But, in a highly heterogeneous system with surface adsorption, chemisorption, ion exchange, precipitation, and intra-particle diffusion processes occur concurrently.<sup>47</sup> Since the modified Zr-based MOF is a porous material with a heterogeneous surface and various active adsorption sites, the kinetic data were fitted to the IPD model to study the role of diffusion in the Hg(II) adsorption process. It is well known that the intra-particle diffusion process consists of three steps: mass transfer, adsorption, and diffusion.<sup>16,44</sup> The data were fitted in two regions, which were regarded as two adsorption processes (Fig. 6d). The calculated rate constant ( $K_{ip}$ ) was in the order of  $K_{ip1} > K_{ip2}$  (Table S10<sup>†</sup>). In the first step ( $K_{ip1}$ ), the adsorption process started with Hg(II) ions migrating from the bulk aqueous phase to the Zr-MOF@Fe<sub>3</sub>O<sub>4</sub> surface. The second step ( $K_{ip2}$ ) occurred after the saturation of the external surface. After saturation of external sites, Hg(II) ions entered the MOF pores with increasing resistance to diffusion. The Hg(II) diffusion into the pores of the Zr-

MOF was limited or partially hindered due to Zr-MOF cavity modification with Fe<sub>3</sub>O<sub>4</sub> nanoparticles. In this study, the mass transfer process was completed in a short time; thus, the ion migration process (first step) and adsorption process (second step) were the main steps of intra-particle diffusion. The data showed that the restrictive step of Hg ion removal by Zr-MOF@Fe<sub>3</sub>O<sub>4</sub> was the adsorption process, not the diffusion process.

The trend between the adsorption amount and the metal ion concentration and how the metal ions interact with the adsorbent were studied using adsorption isotherms. Langmuir, Freundlich, Dubinin–Radushkevich and Temkin isotherm models were applied to analyze the experimental adsorption data. The non-linear adsorption isotherm equations are presented in Table S11.<sup>†</sup> The curves fitted by the models are shown in Fig. 6e and f. The calculated parameters from models are summarized in Table S12.<sup>†</sup> The correlation coefficient ( $R^2$ ) of the Freundlich model (0.99) was higher than those of the Langmuir (0.97), D–R (0.95), and Temkin (0.88) models, indicating that the adsorption process was multilayer adsorption.<sup>16,41</sup> This suggested that the physicochemical forces over the MOF surface play the primary role in the Hg(II) adsorption. The separation factor ( $R_L$ ) computed from the Langmuir model remained between 0 and 1, suggesting a favourable Hg(II) adsorption process over Zr-MOF@Fe<sub>3</sub>O<sub>4</sub>. Moreover, the free Gibbs energy value was negative, which confirmed the spontaneity of the adsorption process.<sup>48</sup> Additionally, the nature of the Hg(II) adsorption process, either physisorption or chemisorption, can be distinguished from the D–R model's free energy ( $E$ ). For  $E < 8$  kJ mol<sup>-1</sup>, the sorption proceeds by physisorption, while for  $E \sim 8$ –16 kJ mol<sup>-1</sup>, the sorption process is driven by chemical forces.<sup>49</sup> The free energy from the D–R model was 9.2 kJ mol<sup>-1</sup>, which indicated that the Hg(II) adsorption process over Zr-MOF@Fe<sub>3</sub>O<sub>4</sub> was multilayer adsorption driven by physicochemical forces.

### Adsorption mechanism

The FTIR spectra of fresh and spent Zr-MOF@Fe<sub>3</sub>O<sub>4</sub> are shown in Fig. 7a. The intensity of the band at 1707 cm<sup>-1</sup> for free –COOH groups diminished after Hg(II) adsorption. The decreased intensity was due to Hg(II) ion binding with the free carboxylic group. This Hg(II)-bound carboxylate group was observed as a new band at 1653 cm<sup>-1</sup>. The band at 3397 cm<sup>-1</sup> for OH stretching in adsorbed water molecules and Zr–OH groups lost intensity in the Hg(II)-adsorbed MOF. The decreased intensity was due to the interaction of Hg(II) ions with the Zr–OH groups upon deprotonation at pH 6. Thus, the FTIR predicted the involvement of free –COOH and Zr–OH groups in the adsorption of Hg(II) ions. The XPS analysis of the spent adsorbent confirmed the presence of 0.7% of Hg ions (Table S3<sup>†</sup>). The HRXPS Hg 4f spectrum has a peak at 100.8 eV, which was assigned to the Hg 4f<sub>7/2</sub> for Hg(II) ions (Fig. 7b).<sup>50</sup> The HRXPS Zr 3d spectrum of the spent adsorbent has two peaks at 183.2 and 185.6 eV, assigned to the 3d<sub>5/2</sub> and 3d<sub>3/2</sub> peaks, respectively. The Zr 3d<sub>5/2</sub> peak in the fresh adsorbent was observed at 182.9 eV. The blue shift of 0.3 eV in the binding energy of the Zr 3d<sub>5/2</sub>





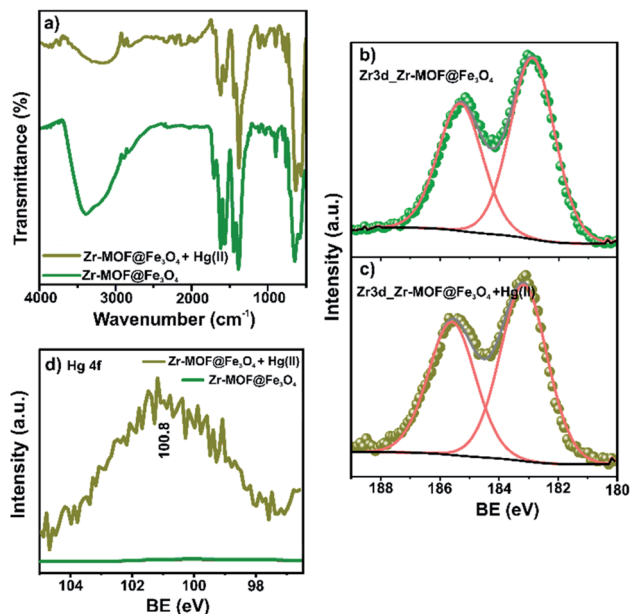


Fig. 7 (a) FTIR spectra; XPS Zr 3d high-resolution signals before (b) and after (c) Hg(II) adsorption. (d) Hg 4f high-resolution signals before and after Hg(II) adsorption.

peak was due to the change in the electron density around Zr after interaction of Hg(II) ions with the deprotonated Zr-OH sites (Fig. 7c). Thus, free carboxylic acid groups and Zr-OH were responsible for Hg(II) adsorption over the magnetic Zr-MOF. This peak was absent in the pristine sample, which confirmed the Hg(II) adsorption process over the magnetic MOF composite (Fig. 7d).

### Reusability

For practical applications, reusability is a crucial factor, which profoundly impacts the sustainability and affordability of the developed adsorbent. In the present study, we have adopted the use of 0.1 mol L<sup>-1</sup> NaOH (Fig. 8a) or HCl (Fig. 8b) solution for stripping Hg(II) ions from the loaded composite. The sorbed Hg(II) ions could be stripped using strong acidic solutions due to the competitive nature of protons for the adsorption sites.<sup>51,52</sup> In the first cycle, the regeneration of the spent composite using the HCl solution desorbed 72% of the adsorbed Hg(II) ions. The desorption efficiency remained in the 63–71% range for the next four cycles. The partial desorption using HCl was due to the significantly high adsorption capacity of the composite at pH 2, which severely limited the desorption process at pH 1. Though the desorption efficiency was less satisfactory, the adsorption capacity of 49.2 mg g<sup>-1</sup> in the first cycle reached 44.7 mg g<sup>-1</sup> in the fifth cycle (~10% drop), suggesting appreciable reusability of the composite. In the reported work on Hg(II) adsorption on Zr-based MOFs, it has been observed that the adsorption capacity tends to drop in a basic solution.<sup>40,44</sup> Thus, the use of a highly basic eluent solution could be effective in the regeneration of the spent adsorbent. The pH 13 solution was highly effective in stripping sorbed Hg(II) ions, where the desorption efficiency remained in the range of 94–97% for five cycles.

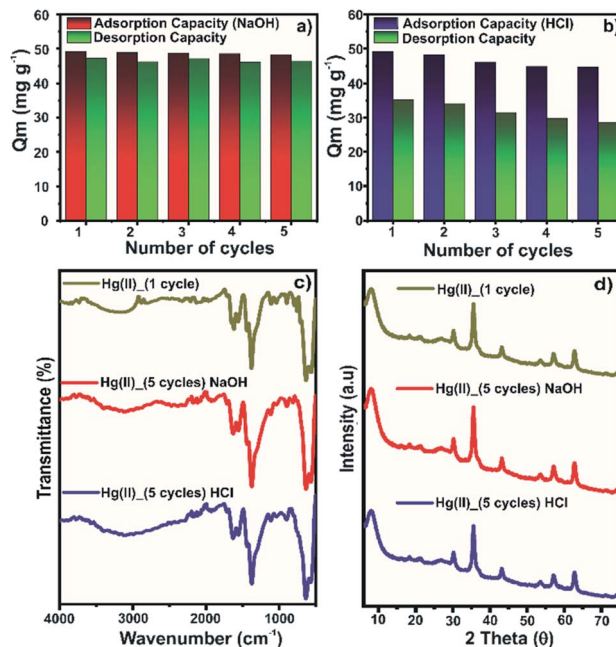


Fig. 8 Regeneration and reusability tests of Zr-MOF@Fe<sub>3</sub>O<sub>4</sub> for the removal of Hg(II) with (a) NaOH eluent and (b) HCl eluent; (c) FTIR spectra; (d) PXRD patterns of Zr-MOF@Fe<sub>3</sub>O<sub>4</sub> after reusability tests. Conditions: mass of Zr-MOF@Fe<sub>3</sub>O<sub>4</sub> = 30 mg, [Hg(II)] = 50 mg L<sup>-1</sup>, [NaOH]/[HCl] = 0.1 mol L<sup>-1</sup>, volume = 30 mL, time = 12 h.

Moreover, the adsorption capacity of 49.2 mg g<sup>-1</sup> in the first cycle dropped by ~1.8% in the fifth cycle. Thus, it was evident that the NaOH solution was highly efficient for regeneration purposes.

The material stability after five adsorption–desorption cycles was assessed by FTIR (Fig. 8c) and PXRD (Fig. 8d) analysis. In the FTIR spectra of regenerated samples, an insignificant change in the band intensity was observed. Only the band at ~1620 cm<sup>-1</sup> for asymmetric stretching of the Zr-COO linkage showed a slight decrease in the intensity, probably due to the breakage of some coordinative bonds. The PXRD diffraction patterns of regenerated samples for five cycles were identical to those of the sample of the first adsorption cycle. Thus, the spectroscopic evidence further confirmed the stability of the composite for multiple Hg(II) adsorption–desorption cycles.

## Conclusions

In this work, we have synthesized a magnetic Zr-MOF to remove toxic metal ions from water. The synthesis of Zr-MOF@Fe<sub>3</sub>O<sub>4</sub> was confirmed through microscopic and spectroscopic techniques such as SEM, FT-IR, Raman, DRX, TGA, and VSM. The Zr-MOF@Fe<sub>3</sub>O<sub>4</sub> showed the maximum Hg(II) uptake capacity of 303 mg g<sup>-1</sup>, which was higher than that of the reported Zr-MOF in the literature, and with an easy phase separation process after adsorption. The Hg(II) adsorption process was driven by physicochemical forces, which were inferred from the fitting of kinetic and adsorption data in the Elovich and Langmuir model, respectively. The mechanism of adsorption was identified by FTIR and XPS analyses, which confirmed the



involvement of  $-\text{COOH}$  and  $\text{Zr-OH}$  groups in the  $\text{Hg(II)}$  adsorption process.  $\text{Zr-MOF}@Fe_3O_4$  showed a simultaneous high uptake capacity of 45.1, 42.9, and 44.2  $\text{mg g}^{-1}$  for  $\text{Hg(II)}$ ,  $\text{Cd(II)}$ , and  $\text{Pb(II)}$ , respectively in a multi-element study. The spent MOF was successfully regenerated by 0.1  $\text{mol L}^{-1}$   $\text{NaOH}$  solution with the retention of 90% of its initial adsorption capacity after 5 cycles. Thus, the study demonstrated a novel magnetic Zr-MOF as a potential candidate for decontaminating heavy metal-rich wastewater.

## Author contributions

R. P. oversaw data curation, formal analysis, and methodology. H. V. and N. K. G. oversaw conceptualization, visualization, software, validation, writing – original draft, and writing – review & editing. A. R.-G. and C. L. were responsible for funding acquisition, investigation, project administration, resources, and supervision.

## Conflicts of interest

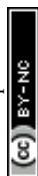
There are no conflicts to declare.

## Acknowledgements

The authors would like to thank Laboratorio Nacional de Ciencia, Tecnología y Gestión Integrada del Agua (LNAGUA) and LNCAE (Laboratorio Nacional de Conversión y Almacenamiento de Energía) for their experimental and instrumental facilities.

## References

- 1 Y. Y. Xiong, J. Q. Li, L. Le Gong, X. F. Feng, L. N. Meng, L. Zhang, P. P. Meng, M. B. Luo and F. Luo, Using MOF-74 for  $\text{Hg}^{2+}$  removal from ultra-low concentration aqueous solution, *J. Solid State Chem.*, 2017, **246**, 16–22.
- 2 P. B. Tchounwou, W. K. Ayensu, N. Ninashvili and D. Sutton, Review: Environmental exposure to mercury and its toxicopathologic implications for public health, *Environ. Toxicol.*, 2003, **18**, 149–175.
- 3 G. K. Kinuthia, V. Ngunjiri, D. Beti, R. Lugalia, A. Wangila and L. Kamau, Levels of heavy metals in wastewater and soil samples from open drainage channels in Nairobi, Kenya: community health implication, *Sci. Rep.*, 2020, **10**, 8434.
- 4 W. Yang, K. Cheng, R. Tang, S. Wu, H. Wang, Z. Han, E. Liu, S. Zhu and L. Che, Ion exchange resin derived magnetic activated carbon as recyclable and regenerable adsorbent for removal of mercury from flue gases, *J. Energy Inst.*, 2021, **97**, 225–232.
- 5 S. Azat, E. Arkhangelsky, T. Papathanasiou, A. A. Zorpas, A. Abirov and V. J. Inglezakis, Synthesis of biosourced silica-Ag nanocomposites and amalgamation reaction with mercury in aqueous solutions, *C. R. Chim.*, 2020, **23**, 77–92.
- 6 Q. Zhang, N. Liu, Y. Cao, W. Zhang, Y. Wei, L. Feng and L. Jiang, A facile method to prepare dual-functional membrane for efficient oil removal and in situ reversible mercury ions adsorption from wastewater, *Appl. Surf. Sci.*, 2018, **434**, 57–62.
- 7 A. Pohl, Removal of heavy metal ions from water and wastewaters by sulfur-containing precipitation agents, *Water, Air, Soil Pollut.*, 2020, **231**, 1–17.
- 8 L. Hao, N. Wang, C. Wang and G. Li, Arsenic removal from water and river water by the combined adsorption-UF membrane process, *Chemosphere*, 2018, **202**, 768–776.
- 9 Z. Liu, D. Liu, B. Zhao, L. Feng, M. Ni and J. Jin, Mercury removal based on adsorption and oxidation by fly ash: A review, *Energy Fuels*, 2020, **34**, 11840–11866.
- 10 N. K. Gupta and A. Gupta, 2D and 3D carbon-based adsorbents for an efficient removal of  $\text{Hg}^{\text{II}}$  ions: A review, *FlatChem*, 2018, **11**, 1–14.
- 11 H. Viltres, Y. C. López, N. K. Gupta, C. Leyva, R. Paz, A. Gupta and A. Sengupta, Functional metal-organic frameworks for metal removal from aqueous solutions, *Sep. Purif. Rev.*, 2022, **51**, 78–99.
- 12 S. Ploychompoo, J. Chen, H. Luo and Q. Liang, Fast and efficient aqueous arsenic removal by functionalized MIL-100(Fe)/rGO/ $\delta$ - $\text{MnO}_2$  ternary composites: Adsorption performance and mechanism, *J. Environ. Sci.*, 2020, **91**, 22–34.
- 13 Q. Liu, Q. Zhang, B. Liu and J. Ma, A new synthesis and adsorption mechanism of  $\text{ZrO}_2$  based metal-organic frames for efficient removal of mercury ions from aqueous solution, *Ceram. Int.*, 2019, **45**, 15720–15724.
- 14 Y. Peng, H. Huang, Y. Zhang, C. Kang, S. Chen, L. Song, D. Liu and C. Zhong, A versatile MOF-based trap for heavy metal ion capture and dispersion, *Nat. Commun.*, 2018, **91**, 187.
- 15 J. E. Efome, D. Rana, T. Matsuura and C. Q. Lan, Insight studies on metal-organic framework nanofibrous membrane adsorption and activation for heavy metal ions removal from aqueous solution, *ACS Appl. Mater. Interfaces*, 2018, **10**, 18619–18629.
- 16 R. Paz, H. Viltres, N. K. Gupta and C. Leyva, Fabrication of magnetic cerium-organic framework-activated carbon composite for charged dye removal from aqueous solutions, *J. Mol. Liq.*, 2021, **337**, 116578.
- 17 H. Furukawa, F. Gándara, Y.-B. Zhang, J. Jiang, W. L. Queen, M. R. Hudson and O. M. Yaghi, Water adsorption in porous metal-organic frameworks and related materials, *J. Am. Chem. Soc.*, 2014, **136**, 4369–4381.
- 18 C. Ardila-Suárez, J. Rodríguez-Pereira, V. G. Baldovino-Medrano and G. E. Ramírez-Caballero, An analysis of the effect of zirconium precursors of MOF-808 on its thermal stability, and structural and surface properties, *CrystEngComm*, 2019, **21**, 1407–1415.
- 19 A. Rajan, M. Sharma and N. K. Sahu, Assessing magnetic and inductive thermal properties of various surfactants functionalised  $\text{Fe}_3\text{O}_4$  nanoparticles for hyperthermia, *Sci. Rep.*, 2020, **10**, 15045.
- 20 S. Biswas, T. Ahnfeldt and N. Stock, New functionalized flexible Al-MIL-53-X ( $X = -\text{Cl}$ ,  $-\text{Br}$ ,  $-\text{CH}_3$ ,  $-\text{NO}_2$ ,  $-(\text{OH})_2$ ) solids: Syntheses, characterization, sorption, and breathing behavior, *Inorg. Chem.*, 2011, **50**, 9518–9526.





- 21 J. Gong, M. J. Katz and F. M. Kerton, Catalytic conversion of glucose to 5-hydroxymethylfurfural using zirconium-containing metal-organic frameworks using microwave heating, *RSC Adv.*, 2018, **8**, 31618–31627.
- 22 N. K. Gupta, S. Kim, J. Bae and K. S. Kim, Chemisorption of hydrogen sulfide over copper-based metal-organic frameworks: methanol and UV-assisted regeneration, *RSC Adv.*, 2021, **11**, 4890–4900.
- 23 C. Ardila-Suárez, A. M. Díaz-Lasprilla, L. A. Díaz-Vaca, P. B. Balbuena, V. G. Baldovino-Medrano and G. E. Ramírez-Caballero, Synthesis, characterization, and post-synthetic modification of a micro/mesoporous zirconium-tricarboxylate metal-organic framework: towards the addition of acid active sites, *CrystEngComm*, 2019, **21**, 3014–3030.
- 24 V. A. J. Silva, P. L. Andrade, M. P. C. Silva, A. D. Bustamante, L. De Los Santos Valladares and J. Albino Aguiar, Synthesis and characterization of Fe<sub>3</sub>O<sub>4</sub> nanoparticles coated with fucan polysaccharides, *J. Magn. Magn. Mater.*, 2013, **343**, 138–143.
- 25 M. Todaro, A. Alessi, L. Sciortino, S. Agnello, M. Cannas, F. M. Gelardi and G. Buscarino, Investigation by Raman spectroscopy of the decomposition process of HKUST-1 upon exposure to air, *J. Spectrosc.*, 2016, **2016**, 8074297.
- 26 K. Doloi, A. Kumar and M. N. Rao, Study of polymerization dynamics in micropores of metal-organic framework, *AIP Conf. Proc.*, 2020, **2265**, 030013.
- 27 K. Knozowska, R. Thür, J. Kujawa, I. Kolesnyk, I. F. J. Vankelecom and W. Kujawski, Fluorinated MOF-808 with various modulators to fabricate high-performance hybrid membranes with enhanced hydrophobicity for organic-organic pervaporation, *Sep. Purif. Technol.*, 2021, **264**, 118315.
- 28 E. Plessers, G. Fu, C. Y. X. Tan, D. E. De Vos and M. B. J. Roeffaers, Zr-based MOF-808 as Meerwein-Ponndorf-Verley reduction catalyst for challenging carbonyl compounds, *Catalysts*, 2016, **6**, 104.
- 29 E. T. Tenório-Neto, T. Jamshaid, M. Eissa, M. H. Kunita, N. Zine, G. Agusti, H. Fessi, A. E. El-Salhi and A. Elaissari, TGA and magnetization measurements for determination of composition and polymer conversion of magnetic hybrid particles, *Polym. Adv. Technol.*, 2015, **26**, 1199–1208.
- 30 A. E. Baumann, J. R. Downing, D. A. Burns, M. C. Hersam and V. S. Thoi, Graphene-metal-organic framework composite sulfur electrodes for Li-S batteries with high volumetric capacity, *ACS Appl. Mater. Interfaces*, 2020, **12**, 37173–37181.
- 31 R. Xu, Q. Ji, P. Zhao, M. Jian, C. Xiang, C. Hu, G. Zhang, C. Tang, R. Liu, X. Zhang and J. Qu, Hierarchically porous UiO-66 with tunable mesopores and oxygen vacancies for enhanced arsenic removal, *J. Mater. Chem. A*, 2020, **8**, 7870–7879.
- 32 N. K. Gupta, Y. Ghaffari, J. Bae and K. S. Kim, Synthesis of coral-like  $\alpha$ -Fe<sub>2</sub>O<sub>3</sub> nanoparticles for dye degradation at neutral pH, *J. Mol. Liq.*, 2020, **301**, 112473.
- 33 A. P. Grosvenor, B. A. Kobe, M. C. Biesinger and N. S. McIntyre, Investigation of multiplet splitting of Fe 2p XPS spectra and bonding in iron compounds, *Surf. Interface Anal.*, 2004, **36**, 1564–1574.
- 34 S. Pourbeyram, Effective removal of heavy metals from aqueous solutions by graphene oxide-zirconium phosphate (GO-Zr-P) nanocomposite, *Ind. Eng. Chem. Res.*, 2016, **55**, 5608–5617.
- 35 Y. Liu, X. Liu, W. Dong, L. Zhang, Q. Kong and W. Wang, Efficient adsorption of sulfamethazine onto modified activated carbon: A plausible adsorption mechanism, *Sci. Rep.*, 2017, **7**, 12437.
- 36 N. K. Gupta, M. Saifuddin, S. Kim and K. S. Kim, Microscopic, spectroscopic, and experimental approach towards understanding the phosphate adsorption onto Zn-Fe layered double hydroxide, *J. Mol. Liq.*, 2020, **297**, 111935.
- 37 R. S. El-Tawil, S. T. El-Wakeel, A. E. Abdel-Ghany, H. A. M. Abuzeid, K. A. Selim and A. M. Hashem, Silver/quartz nanocomposite as an adsorbent for removal of mercury (II) ions from aqueous solutions, *Heliyon*, 2019, **5**, E02415.
- 38 A. Gupta, H. Viltres and N. K. Gupta, Sono-adsorption of organic dyes onto CoFe<sub>2</sub>O<sub>4</sub>/Graphene oxide nanocomposite, *Surf. Interfaces*, 2020, **20**, 100563.
- 39 N. Assaad, G. Sabeh and M. Hmadeh, Defect control in Zr-based metal-organic framework nanoparticles for arsenic removal from water, *ACS Appl. Nano Mater.*, 2020, **3**, 8997–9008.
- 40 Z. Seyfi Hasankola, R. Rahimi, H. Shayegan, E. Moradi and V. Safarifard, Removal of Hg<sup>2+</sup> heavy metal ion using a highly stable mesoporous porphyrinic zirconium metal-organic framework, *Inorg. Chim. Acta*, 2020, **501**, 119264.
- 41 Y. Zhao, D. Wang, W. Wei, L. Cui, C.-W. Cho and G. Wu, Effective adsorption of mercury by Zr(IV)-based metal-organic frameworks of UiO-66-NH<sub>2</sub> from aqueous solution, *Environ. Sci. Pollut. Res.*, 2020, **28**, 7068–7075.
- 42 S. Chen, F. Feng, S. Li, X.-X. Li and L. Shu, Metal-organic framework DUT-67 (Zr) for adsorptive removal of trace Hg<sup>2+</sup> and CH<sub>3</sub>Hg<sup>+</sup> in water, *Chem. Speciation Bioavailability*, 2018, **30**, 99–106.
- 43 P. Yang, Y. Shu, Q. Zhuang, Y. Li and J. Gu, A robust MOF-based trap with high-density active alkyl thiol for the super-efficient capture of mercury, *Chem. Commun.*, 2019, **55**, 12972–12975.
- 44 L. Fu, S. Wang, G. Lin, L. Zhang, Q. Liu, J. Fang, C. Wei and G. Liu, Post-functionalization of UiO-66-NH<sub>2</sub> by 2,5-Dimercapto-1,3,4-thiadiazole for the high efficient removal of Hg(II) in water, *J. Hazard. Mater.*, 2019, **368**, 42–51.
- 45 J. Li, Y. Liu, Y. Ai, A. Alsaedi, T. Hayat and X. Wang, Combined experimental and theoretical investigation on selective removal of mercury ions by metal organic frameworks modified with thiol groups, *Chem. Eng. J.*, 2018, **354**, 790–801.
- 46 L. Ding, X. Luo, P. Shao, J. Yang and D. Sun, Thiol-functionalized Zr-based metal-organic framework for capture of Hg(II) through a proton exchange reaction, *ACS Sustainable Chem. Eng.*, 2018, **6**, 8494–8502.
- 47 K. Riahi, S. Chaabane and B. Ben Thayer, A kinetic modeling study of phosphate adsorption onto Phoenix *dactylifera* L.



- date palm fibers in batch mode, *J. Saudi Chem. Soc.*, 2017, **21**, S143–S152.
- 48 M. Chiban, G. Carja, G. Lehtu and F. Sinan, Equilibrium and thermodynamic studies for the removal of As(V) ions from aqueous solution using dried plants as adsorbents, *Arabian J. Chem.*, 2016, **9**, S988–S999.
- 49 N. K. Gupta, A. Gupta, P. Ramteke, H. Sahoo and A. Sengupta, Biosorption-a green method for the preconcentration of rare earth elements (REEs) from waste solutions: A review, *J. Mol. Liq.*, 2019, **274**, 148–164.
- 50 V. Chandra and K. S. Kim, Highly selective adsorption of  $\text{Hg}^{2+}$  by a polypyrrole-reduced graphene oxide composite, *Chem. Commun.*, 2011, **47**, 3942–3944.
- 51 S. Venkateswarlu and M. Yoon, Rapid removal of cadmium ions using green-synthesized  $\text{Fe}_3\text{O}_4$  nanoparticles capped with diethyl-4-(4-amino-5-mercapto-4H-1,2,4-triazol-3-yl) phenyl phosphonate, *RSC Adv.*, 2015, **5**, 65444–65453.
- 52 Z. Ramezani, N. Pourmand, A. Behfar and A. Momeni, Removal and recovery of mercury from chlor-alkali petrochemical wastes using  $\gamma\text{-Fe}_2\text{O}_3$  nanoparticles, *Appl. Petrochem. Res.*, 2016, **6**, 403–411.

